A Surgical Robot for Intracorporeal Additive Manufacturing of Tissue Engineering Constructs

Andrej Simeunović D, Kevin Wolf, Kollin Tierling, and David J. Hoelzle D

Abstract—The confluence of additive manufacturing (AM) based tissue engineering (TE), termed bioprinting, and robotic-assisted surgery (RAS) has the potential to increase the clinical adoption of regenerative medicine therapies by bioprinting inside the body. However, existing in vivo bioprinting systems are lacking in achievable structural complexity, defect access, or procedure invasiveness as they do not leverage the form factors of commercial RAS systems. Translating AM to RAS increases fluid pressures considerably, in turn increasing cell damage and decreasing cellular proliferation in TE constructs. Here, we describe Endoscopic AM, an intracorporeal bioprinting system that mimics the designs of commercial RAS systems and that has a novel endoscopic material metering system that produces cell pressures comparable to benchtop AM bioprinters. We present Endoscopic AM's design, kinematics, fluid dynamics, and compare printing in a human body model to benchtop printing. We demonstrate intracorporeal printing is approximately 5 times less accurate than benchtop printing at this current design iteration, but that structure fidelity is sufficient for TE requirements.

Index Terms—Additive manufacturing, mechanism design, medical robots and systems, surgical robotics: laparoscopy.

I. INTRODUCTION

B IOPRINTING, the use of additive manufacturing (AM) for tissue engineering (TE), has made significant progress in the laboratory setting, but continues to be challenged in the clinical setting [1]–[5]. In the clinic, construct delivery is particularly problematic, as TE constructs are printed outside the body (extracorporeally), requiring an open surgery for placement at the tissue defect inside the body (intracorporeally). Open surgeries increase morbidities over minimally invasive procedures [6]–[10] and, for simple TE constructs, these morbidities often negate their therapeutic benefits, impeding clinical adoption of TE. In parallel, robotic-assisted surgery (RAS) systems have brought articulating, robotically controlled, minimally invasive

Manuscript received February 24, 2022; accepted June 10, 2022. Date of publication June 17, 2022; date of current version June 27, 2022. This letter was recommended for publication by Associate Editor E. De Momi and Editor P. Valdastri upon evaluation of the reviewers' comments. This work was supported in part by NSF CAREER under Grant CMMI-1708819, in part by NSF GRFP under Grant DGE-1343012, and in part by NSF PFI under Grant IIP-1919204. (Corresponding author: Andrej Simeunović.)

Andrej Simeunović, Kevin Wolf, and David J. Hoelzle are with the Department of Mechanical and Aerospace Engineering, The Ohio State University, Columbus, OH 43210 USA (e-mail: simeunovic.1@osu.edu; wolf.530@osu.edu; hoelzle.1@osu.edu).

Kollin Tierling is with Intuitive Surgical, Inc., Sunnyvale, CA 94086 USA (e-mail: kollin.tierling@intusurg.com).

This letter has supplementary downloadable material available at https://doi.org/10.1109/LRA.2022.3183752, provided by the authors.

Digital Object Identifier 10.1109/LRA.2022.3183752

surgical instruments into nearly every surgical domain [11], [12]. Critically, the designs of RAS systems are amenable to integration with TE fabrication systems, providing the opportunity for material delivery minimally invasively. Taken together, we can consider the confluence of RAS and bioprinting, resulting in a minimally invasive, endoscopic bioprinting system that is capable of clinically relevant fabrication intracorporeally (Fig. 1).

Previous works in in vivo bioprinting that leverage minimally invasive methods [13]-[15] show promise for realizing facets of intracorporeal TE, but are limited in their achievable structural complexity, defect access, or procedure invasiveness. Accordingly, we seek to integrate TE fabrication into existing commercial RAS designs to better meet these requirements and to further drive the clinical adoption of TE based regenerative medicine therapies. From the AM perspective, extrusion-based methods (direct-write AM, DW) are the only ones compatible with the intracorporeal environment, but translating benchtop DW to an endoscopic form factor increases fluid pressure significantly (>10× benchtop DW) [16]. Increasing the pressure experienced by cells in the build material increases cell damage and decreases cellular proliferation in TE constructs [17]-[20]. For example, if benchtop pressures (150 kPa) are doubled, cell damage increases from 10% to 25% [21]. Accordingly, we seek to decouple the increased pressures required to meter material in endoscopic DW with that experienced by embedded cells.

Here, we describe a minimally invasive intracorporeal bioprinting system, Endoscopic AM, that mimics the design of commercial RAS systems and has a novel, hydraulically driven material metering system that allows for build material fluid pressures comparable to benchtop systems (170 kPa). We detail the system's design, kinematics, and fluid dynamics, and compare its ability to print structures intracorporeally in a RAS human body model to a benchtop bioprinting system. We find that Endoscopic AM printing fidelity is approximately 5 times less accurate than a benchtop system, but still satisfies the needs for intracorporeal structure fabrication.

II. SYSTEM DESIGN

Endoscopic AM is a custom designed 8-degree of freedom (DOF) open serial kinematic chain manipulator composed of: 1) a 5-DOF arm, termed the endoscopic arm, and 2) a positive-displacement direct-write (DW) endoscopic extruder, termed the microextrusion tool (Fig. 2). The endoscopic arm positions the microextrusion tool and maintains a remote center of motion (RCM), a fulcrum midway through the kinematic chain, located

2377-3766 © 2022 IEEE. Personal use is permitted, but republication/redistribution requires IEEE permission. See https://www.ieee.org/publications/rights/index.html for more information.

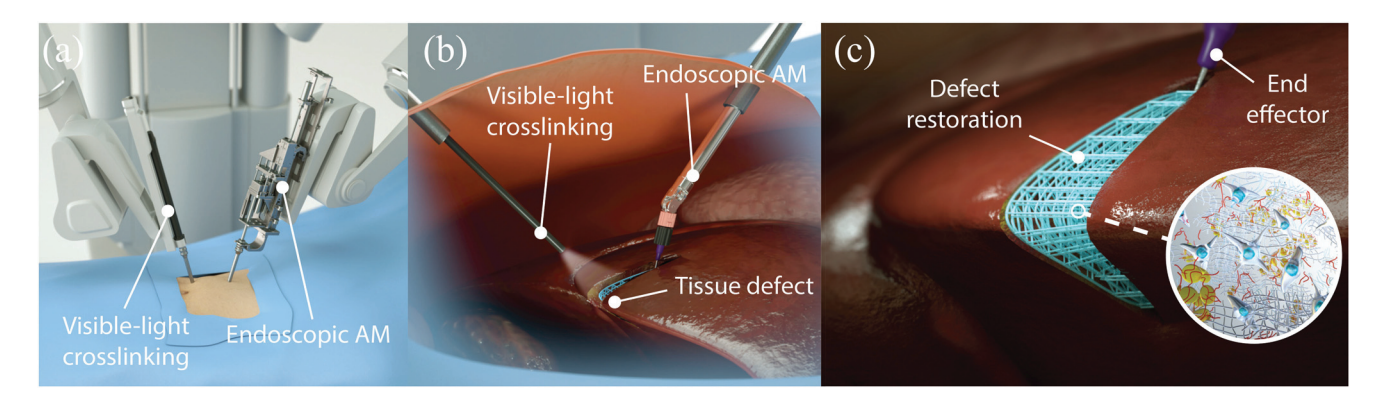


Fig. 1. Concept of intracorporeal tissue engineering with Endoscopic AM. (a), (b) The Endoscopic AM system allows for printing of synthetic tissue structures in the body through standard minimally invasive surgical ports. (c) Intracorporeal tissue engineering allows surgeons to print tissue structures at the surgical site. Inset: materials in Endoscopic AM are biomaterials embedded with cells, growth factors, and other biologics.

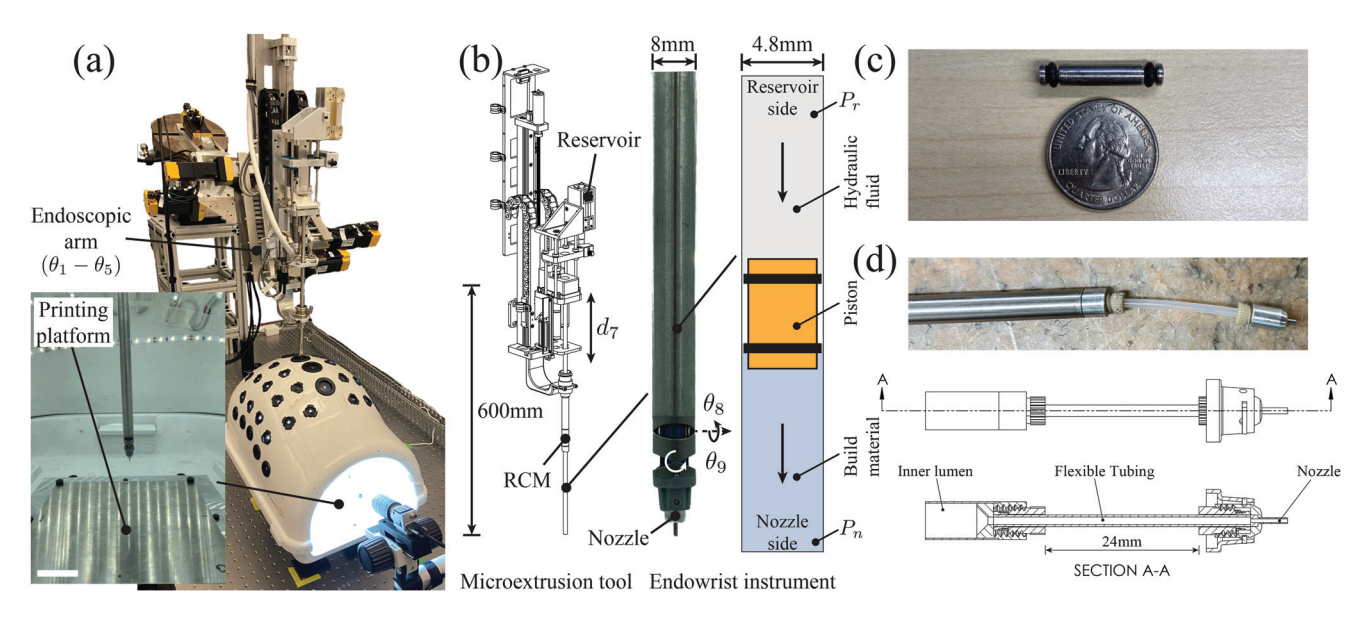


Fig. 2. Endoscopic AM system overview. (a) Endoscopic AM system. Inset: mock intracorporeal environment. Scale bar is 25 mm. (b) Microextrusion tool and modified da Vinci Xi Endowrist Suction-Irrigator instrument within tool. The hydraulically driven material metering system is inside the Suction-Irrigator inner lumen. (c) Piston in the material metering system. (d) Custom nozzle assembly to deliver material through the instrument wrist.

at the body entry point. Positioning in the body is achieved with a 1-DOF prismatic joint for body insertion and an articulating end-effector based on a modified da Vinci instrument with a 2-DOF wrist. Material delivery is accomplished with a hydraulically driven fluid system that keeps the hydraulic material reservoir and motors extracorporeal and maintains material pressures safe for cells.

A. Mechanical Design

The 5 joints of the endoscopic arm $(\theta_1 - \theta_5)$, Fig. 2(a)) are kinematically constrained to achieve a RCM for safe intracorporeal operation, achieving in software analogous operation as that of a RCM mechanism such as a parallelogram. $\theta_1 - \theta_5$ are extracorporeal and several orders of magnitude larger in torque than the intracorporeal joints, $d_7 - \theta_9$, to support the mass of the microextrusion tool and to minimize RCM deflections. The

microextrusion tool consists of a modified da Vinci Xi Endowrist instrument (Suction-Irrigator, # 480299) with an embedded hydraulically driven material metering system (Fig. 2(b)). The wrist of Endowrist instruments is cable driven [22] allowing us to keep the motors of the intracorporeal joints extracorporeal. A prismatic joint, d_7 , in the microextrusion tool determines the depth into the body of the Endowrist instrument.

Due to the instrument's small inner lumen size (\emptyset 4.8 mm), the hydraulic actuator piston floats freely in the inner lumen and prevents material bypass between hydraulic fluid and build material via O-rings (Fig. 2(c)). The hydraulic fluid, a biocompatible fluid such as mineral oil or saline, is controlled by volumetric displacement with a syringe mounted extracorporeally; hydraulic fluid volume changes displace the piston, in turn metering the build material. The inner lumen connects to the nozzle assembly with a short region of flexible PTFE tubing to pass build material through the articulating joints of the wrist (Fig. 2(d)). We use

extrusion nozzle sizes typical for DW AM (e.g., $510 \mu m$) which lead to relative pressures on the order of 170 kPa, and which are comparable to benchtop AM systems [23], [24].

B. Control and Software Architecture

Endoscopic AM runs on a custom software stack consisting of a front-end graphical user interface that controls a Simulink Real-TimeTM executable running on a Speedgoat Target computer, which acts as the master node for a network of servo drives that perform individual motor control. Signal synchronization is achieved via the EtherCAT industrial fieldbus [25] with the Target computer as the EtherCAT master node. All servo drives have a CANopen CiA 402 series device profile [26], allowing for a fast response and shutdown protocol for high priority faults, and relegates system critical operation to high-performance FPGA hardware, minimizing the computational overhead on the comparably slower Matlab software running on the host computer.

Trajectories are generated in Cartesian space as a primary requirement of printing is near constant nozzle velocity. Trajectories consist of linear segments with parabolic blends (LSPBs) with moderate coast velocity to acceleration ratio (1:25) to minimize vibrations. For a given move, a one-dimensional LSPB of the norm of end effector position, s(t), is defined. Linear interpolations in position and SLERP interpolations in quaternions [27] between the move start and end points are time scaled, x(s(t)) and q(s(t)) respectively, to achieve a synchronized LSPB in Cartesian space. If position distance is zero or if the orientation acceleration limit would be exceeded, the time scaling is based upon the orientation distance,

$$D_q = 2\arccos|q_1 \cdot q_2|,\tag{1}$$

where q_1 and q_2 are the quaternion representations of orientation at the start and end points, respectively. Cartesian trajectories are mapped in real-time to the joint space using inverse kinematics, Section III-A. Precise positioning is achieved with an independent joint control network. At each time step, the EtherCAT master sends reference positions to cascaded feedback controllers embedded in each servo drive.

C. Mock Intracorporeal Environment

To mimic the intracorporeal environment, a da Vinci Simulator (Part # 372363) is modified to house interchangeable printing platforms, cameras, and lighting equipment (inset of Fig. 2(a)). The printing platform can be changed to various surface geometries to mimic natural tissues and can be mounted to angled fixtures to better represent anatomical positioning. Materials with mechanical properties in the soft tissue range, such as chicken strips and 2% agarose (#A4018, Sigma Aldrich), can be used to mimic soft tissue substrates [28]. Fixturing printed structures to soft tissues is particularly challenging, and we have previously demonstrated a pierce-and-overextrude method to adhere printed synthetic soft tissues to soft-tissue mimics with a DW system [29].

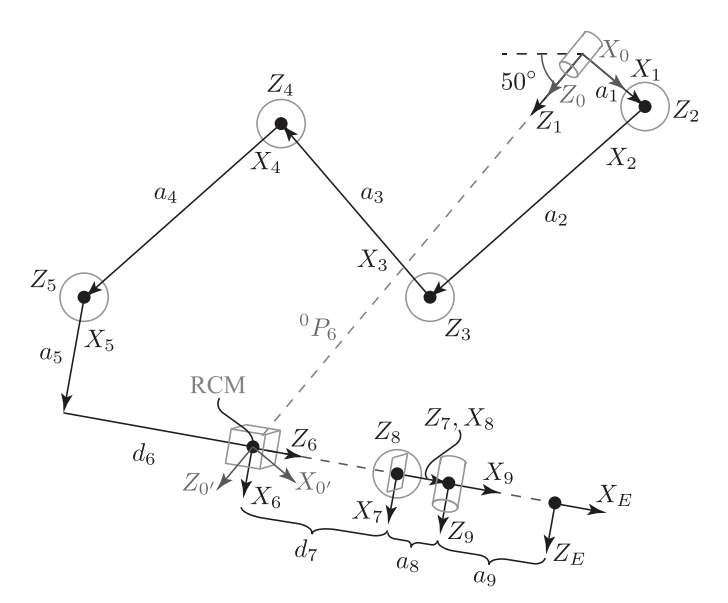


Fig. 3. Schematic of kinematics.

TABLE I
D-H PARAMETERS. * DENOTES A MOVEABLE JOINT

	i	α_{i-1}	a_{i-1}	d_i	θ_i
Extracorporeal	1	0	0	0	$ heta_1^*$
	2	-90	a_1	0	$ heta_2^*$
	3	0	a_2	0	θ_3^*
	4	0	a_3	0	$ heta_4^*$
	5	0	a_4	0	θ_5^*
RCM	6	-90	a_5	d_6	0
Intracorporeal	7	0	0	d_7^*	0
	8	90	0	0	$ heta_8^*$
	9	90	a_8	0	$ heta_9^*$
	Е	0	a_9	0	0

III. DESIGN ANALYSIS

A. Kinematics

The joint arrangements of Endoscopic AM and da Vinci Xi share the same general architecture to assist with integration with existing RAS workflows. Endoscopic AM consists of five extracorporeal joints (θ_1 - θ_5) and three intracorporeal joints (d_7 - θ_9) demarcated by the RCM located at position 0P_6 (Fig. 3). To make the RCM invariant to joint configurations, 0P_6 is constant and defined by passive joints in the base, fixed prior to operation. In addition to the base frame, $\{0\}$, and the end effector frame, $\{E\}$, the RCM constraint leads to both an intermediary base frame, $\{0'\}$ (the base of the intracorporeal joints), and an intermediary end frame, $\{6\}$ (the end of the extracorporeal joints), located at the RCM.

Denavit-Hartenberg (D-H [30]) parameters are presented in Table I. The extracorporeal joints define two tool shaft angles at the RCM and are constrained in two directions by ${}^{0}P_{6}$ (1 direction is redundant). Thus, the under-constrained 5-DOF

extracorporeal joints provide additional dexterity extracorporeally, where it may be operating near other manipulator arms or personnel in a clinical setting. The 2 tool shaft angles from the extracorporeal joints and the three intracorporeal joints allow for 5-DOF operation intracorporeally, which fully define the end effector, as the nozzle is axisymmetric.

A closed-form solution for the inverse kinematics can be found by applying an artificial constraint to the extracorporeal joints. We use a simple linear constraint,

$$\theta_3 = -\theta_4 + \delta,\tag{2}$$

where δ is a constant offset, but other closed-form solutions are possible with an appropriately selected constraint. Let the position and orientation of the nozzle relative to the RCM be ${}^{0'}P_E = [p_x, p_y, p_z]^{\top}$ and ${}^{0'}_E R = R_z(\alpha)R_y(\beta)R_x(\epsilon)$, respectively. Inverting the intracorporeal joints, ${}^{E}_{0'}T = ({}^{0'}_ET)^{-1}$, to find ${}^{E}P_{0'} = [p'_x, p'_y, p'_z]^{\top}$, yields the inverse kinematics

$$\begin{aligned} \theta_1 &= \mathrm{atan2}(c_{\alpha}c_{\epsilon}s_{\beta}c_8 - c_{\alpha}c_{\beta}c_9s_8 + s_{\alpha}c_8s_{\epsilon} - c_{\epsilon}s_{\alpha}s_8s_9 \\ &+ c_{\alpha}s_{\beta}s_{\epsilon}s_8s_9, c_{\epsilon}s_{\alpha}s_{\beta}c_8 - c_{\alpha}c_8s_{\epsilon} - c_{\beta}s_{\alpha}c_9s_8 \\ &+ c_{\alpha}c_{\epsilon}s_8s_9 + s_{\alpha}s_{\beta}s_{\epsilon}s_8s_9) \\ \theta_2 &= \mathrm{atan2}((a_1 + a_5c_{\lambda} - d_6s_{\lambda})(a_3s_3 + a_4s_{\delta}) - (a_2 + a_3c_3 \\ &+ a_4c_{\delta})(^0P_{6,z} + a_5s_{\lambda} + d_6c_{\lambda}), (a_2 + a_3c_3 + a_4c_{\delta})(d_6s_{\lambda} - a_1 - a_5c_{\lambda}) - (a_3s_3 + a_4s_{\delta})(^0P_{6,z} + a_5s_{\lambda} + d_6c_{\lambda})) \\ \theta_3 &= \mathrm{atan2}\left(G/\rho, \pm \sqrt{1 - (G/\rho)^2}\right) - \mathrm{atan2}(2a_2a_3 \\ &+ 2a_3a_4c_{\delta}, 2a_3a_4s_{\delta}) \\ \theta_4 &= \delta - \theta_3 \\ \theta_5 &= \lambda - (\theta_2 + \delta) \\ d_7 &= \sqrt{(a_8 + (a_9 + p'_x)c_9 - p'_ys_9)^2 + p'_z^2} \\ \theta_8 &= \mathrm{atan2}(-(a_9 + p'_x)c_9 + p'_ys_9 - a_8, p'_z) \\ \theta_9 &= \mathrm{atan2}(0, \pm 1) - \mathrm{atan2}(p'_y, p'_x + a_9), \end{aligned} \tag{3}$$

where

$$\lambda = \operatorname{atan2}(\pm\sqrt{1 - (c_{\beta}c_{\epsilon}c_{8} + s_{\beta}c_{9}s_{8} + c_{\beta}s_{\epsilon}s_{8}s_{9})^{2}},$$

$$c_{\beta}c_{\epsilon}c_{8} + s_{\beta}c_{9}s_{8} + c_{\beta}s_{\epsilon}s_{8}s_{9})$$

$$\rho = \sqrt{(2a_{3}a_{4}s_{\delta})^{2} + (2a_{2}a_{3} + 2a_{3}a_{4}c_{\delta})^{2}}$$

$$G = (-a_{1} - a_{5}c_{\lambda} + d_{6}s_{\lambda})^{2} + ({}^{0}P_{6,z} + a_{5}s_{\lambda} + d_{6}c_{\lambda})^{2} - a_{2}^{2}$$

$$- a_{3}^{2} - a_{4}^{2} - 2a_{2}a_{4}c_{\delta}.$$
(4)

Note that there are eight sets of solutions: two from the extracorporeal joints and four from the intracorporeal joints. The two extracorporeal solutions correspond to an elbow down or elbow up configuration, and it is undesirable to switch between them as this will cause large displacements at high velocities for the largest joints in the system. For simplicity, we operate

only in the elbow down configuration, and choose between the remaining four solutions by first considering joint limits and kinematic singularities, and then selecting between the remaining the solution which minimizes $\|\tilde{\Theta}_i - \tilde{\Theta}_{i-1}\|$, where $\tilde{\Theta}$ are joint positions normalized by their range of motion, and i and i-1 are the current and previous time step. The motors for θ_8 and θ_9 drive dials which actuate cable and pulley mechanisms to achieve the desired joint position. The mapping between dials and joints is given by the system

$$\begin{bmatrix} \theta_{d_8} \\ \theta_{d_9} \end{bmatrix} = \begin{bmatrix} 1 & -1 \\ 1 & 1 \end{bmatrix} \begin{bmatrix} \theta_8 \\ \theta_9 \end{bmatrix}, \tag{5}$$

where θ_i and θ_{d_i} are joint and dial positions, respectively.

B. Fluid Dynamics

Our description of Endoscopic AM fluid dynamics builds upon our previous work for DW AM systems [23], where a lumped parameter model of fluidic capacitance and resistance captures the dominant dynamics relevant for printing (Fig. 4). Fluid line elements with large volumes exhibit fluidic capacitance and elements with small radii exhibit fluidic resistance. As is done with benchtop DW AM systems, the reservoir and nozzle are modeled as a capacitor and resistor, respectively. Conversely, the inner lumen, flexible tube, and inlet tube that connects the reservoir to the inner lumen have both small radii and large volumes due to their length, and thus have both capacitance and resistance. We model these elements as a series of R-C elements.

Hydraulic fluid upstream of the piston (Fig. 2(b)) is Newtonian, and the capacitance and resistance are modeled by

$$C_h = \frac{V}{\beta_h},\tag{6}$$

$$R_h = \frac{8\eta L}{\pi r^4},\tag{7}$$

where β_h is the bulk modulus of the hydraulic fluid, V is the volume of the element, η is the viscosity of the hydraulic fluid, and r and L are the radius and length of the element, respectively. Build material downstream of the piston is non-Newtonian and characteristic of yield-pseudoplastic fluids (YPFs), which are described by the Herschel-Bulkley constitutive equation

$$\tau = \tau_0 + k\dot{\gamma}^n,\tag{8}$$

where for a given shear rate $\dot{\gamma}$, the one-dimensional shear stress along the nozzle central axis, τ , is defined by the yield stress τ_0 , the fluid consistency index k, and the flow behavior index n [31]. Capacitors with YPFs are described by

$$C_b = \frac{V}{\beta_b},\tag{9}$$

where β_b is the bulk modulus of the build material. Flow rate of the build material through elements, Q_b , is equivalent to flow rate of a YPF through a pipe, which is described by (10), where

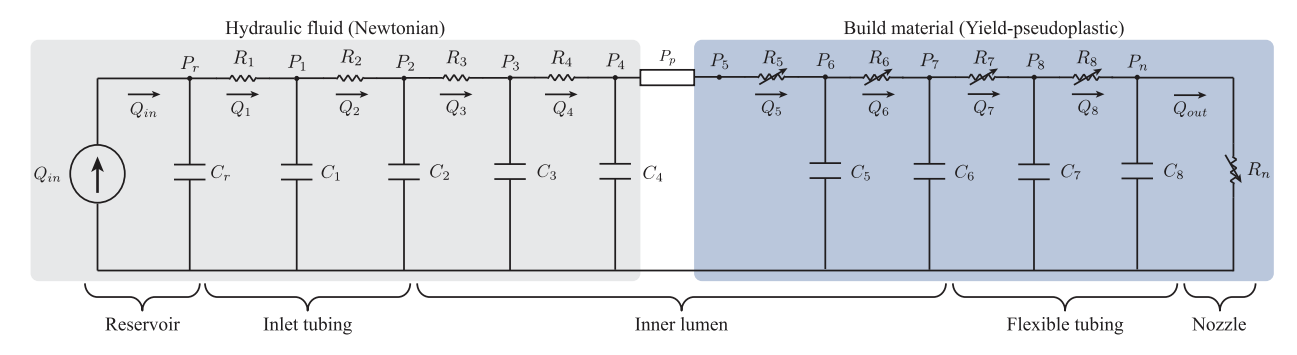


Fig. 4. Fluidic circuit for hydraulically driven microextrusion tool. Flow upstream of the piston is Newtonian. Flow downstream of the piston is non-Newtonian and characteristic of yield-pseudoplastic fluids.

 $\phi = \frac{\tau_0}{\tau_w}$, $\tau_w = \frac{Pr}{2L}$, and P is the pressure drop across the element.

$$Q_{b} = \begin{cases} \pi r^{3} n \left(\frac{\tau_{w}}{k}\right)^{1/n} (1 - \phi)^{(n+1)/n} \\ \times \left[\frac{(1 - \phi)^{2}}{3n + 1} + \frac{2\phi(1 - \phi)}{2n + 1} + \frac{\phi^{2}}{n + 1}\right] & \text{for } \phi \le 1 \\ 0 & \text{for } \phi > 1 \end{cases}$$
(10)

The flow rate through a Newtonian element is simply $Q_h = PR_h$. The pressure drop across any element is given by

$$\dot{P} = \frac{1}{C} \left(Q_i - Q_o \right),\tag{11}$$

where Q_i and Q_o are the flow rate into and out of the element, and C is described by (6) or (9).

The pressure drop across the piston is the pressure required to overcome the static and dynamic seal applied by the O-rings along the length of the piston, which can be found via a force balance across the piston,

$$m\dot{v}_p = P_p A_p - (Bv_p + \mu_s N_p), \qquad (12)$$

where m is piston mass, v_p is piston velocity, P_p is the pressure drop across the piston, A_p is the piston cross-sectional area, B is the viscous friction coefficient, μ_s is the static friction coefficient, and N_p is the normal force acting on the O-rings.

Simulated open loop flow rate and pressure responses for Endoscopic AM and a benchtop DW system are shown in Fig. 5. While reservoir pressure, P_r , is significantly larger in Endoscopic AM, nozzle pressure, P_n , is comparable to the benchtop system. Due to the material metering design, cells embedded in the build material experience only pressures on the order of P_n (Fig. 2(b)).

IV. EXPERIMENTS

To study the intracorporeal fabrication capabilities of Endoscopic AM, we print lattice structures commonly used for TE scaffolds and compare them to equivalent prints with a conventional benchtop bioprinting system with image-based measurements. The benchtop system consists of a DW extruder attached to a XYZ gantry system and has been previously described in [23]. A 20 mm \times 20 mm 1-layer lattice with 2 mm line spacing (Fig. 7(a)) is printed to assess positioning errors and filament consistency. A 4-layer lattice consisting of 2 layers

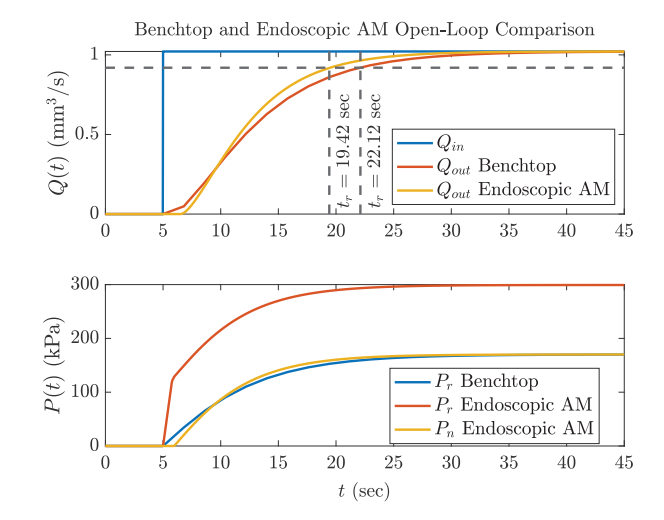


Fig. 5. Simulated open loop flow rate and pressure responses in Endoscopic AM and benchtop DW systems. The two systems have a comparable rise time (Q(t) vs. t) and steady state pressure for build material $(P_r \text{ benchtop}, P_n \text{ Endoscopic AM})$.

identical to the 1-layer lattice and 2 layers of the 1-layer lattice rotated 90° (Fig. 8(a)) is printed to assess porosity fidelity.

All structures are printed at room temperature with a $r_n=0.255~\rm mm$ nozzle radius and $h=0.4~\rm mm$ layer stand-off height on flat platforms (black oxide coated steel for benchtop AM, aluminum for Endoscopic AM). As our primary concern is manufacturability, for both structures, we print 3 examples with Endoscopic AM and 1 example with benchtop AM using a common DW build material, a low yield stress YPF paste, at a nozzle velocity of 5 mm/s. Flow is open loop controlled and lead-in lines are used to develop flow to steady state; excess material is expelled away from the structure upon print completion during the flow transient decay to zero. To account for printing platform positioning errors relative to $\{E\}$, 3 points are measured using the nozzle and used to reconstruct the orientation of the platform relative to $\{E\}$; lattice waypoints are calibrated relative to this plane.

Filament consistency is assessed with measurement of deposited filament width. Filament gaps correspond to separations in flow, typically due to air bubbles. We assume extruded filament takes on the elliptical cross-section in Fig. 6(a), where positioning errors normal to the printing platform (Δz) deform

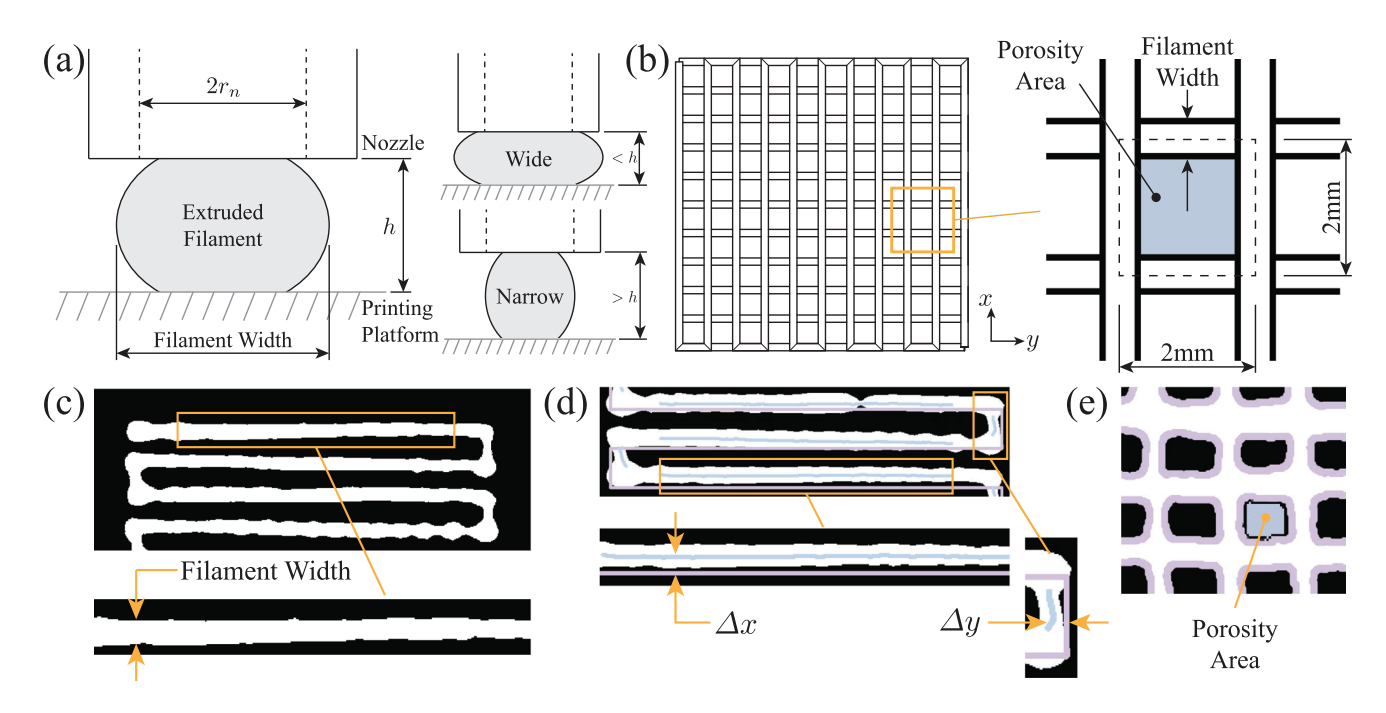


Fig. 6. Structure evaluation methods. (a) Assumed cross-section for filament width. Errors in h deform the extruded filament. (b) Definition of porosity area. (c), (d), (e) Image-based measurement of 1-layer and 4-layer printed structures. 1-layer: filament width and Δx , Δy ; 4-layer: porosity area.

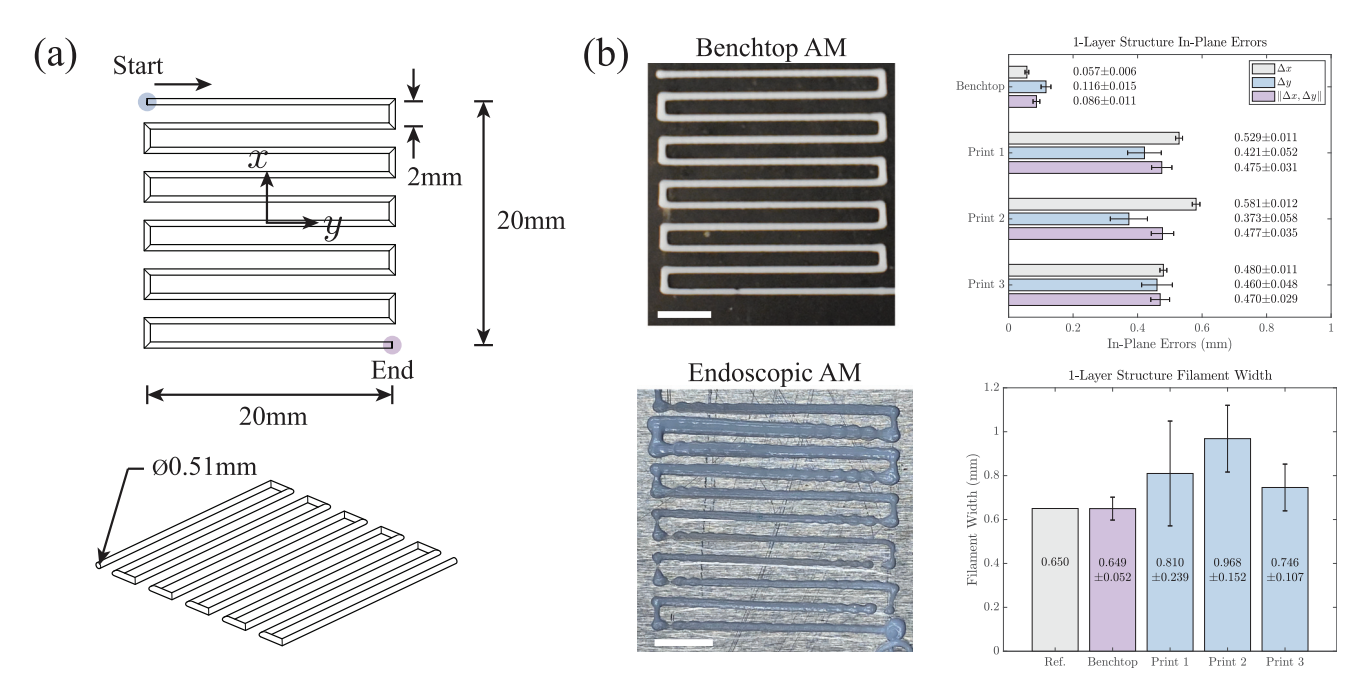


Fig. 7. Single layer lattice structures. (a) Structure design. (b) Printing results for 1 print with benchtop system and 3 prints with Endoscopic AM system. Print 1 is pictured for Endoscopic AM. Numerical results present averaged values with one standard deviation. Scale bars are 5 mm.

the filament [32]. Positioning errors in the printing plane $(\Delta x, \Delta y)$ are measurements of filament center deviations from the reference path. Porosity fidelity is assessed with measurements of porosity area, the inner area between interlocking filament in the 4-layer lattice (Fig. 6(b)).

High-resolution images are taken of completed prints and then binarized, cropped, and straightened. Pixel-to-mm scale is determined from a machinists' ruler placed on the printing platform in the image ($\pm 36.8~\mu m$ per pixel). Filament width is the x distance between the topmost and bottommost white pixel at each y position along each 16 mm wide horizontal segment centered about y=0 (Fig. 6(c)). The 11 horizontal segments in each 1-layer lattice produce an array of filament widths, which is averaged twice $(11\times N\to 1\times N\to 1\times 1)$ to report a scalar filament width per print. Δx errors are deviations along these horizontal segments, and Δy errors are

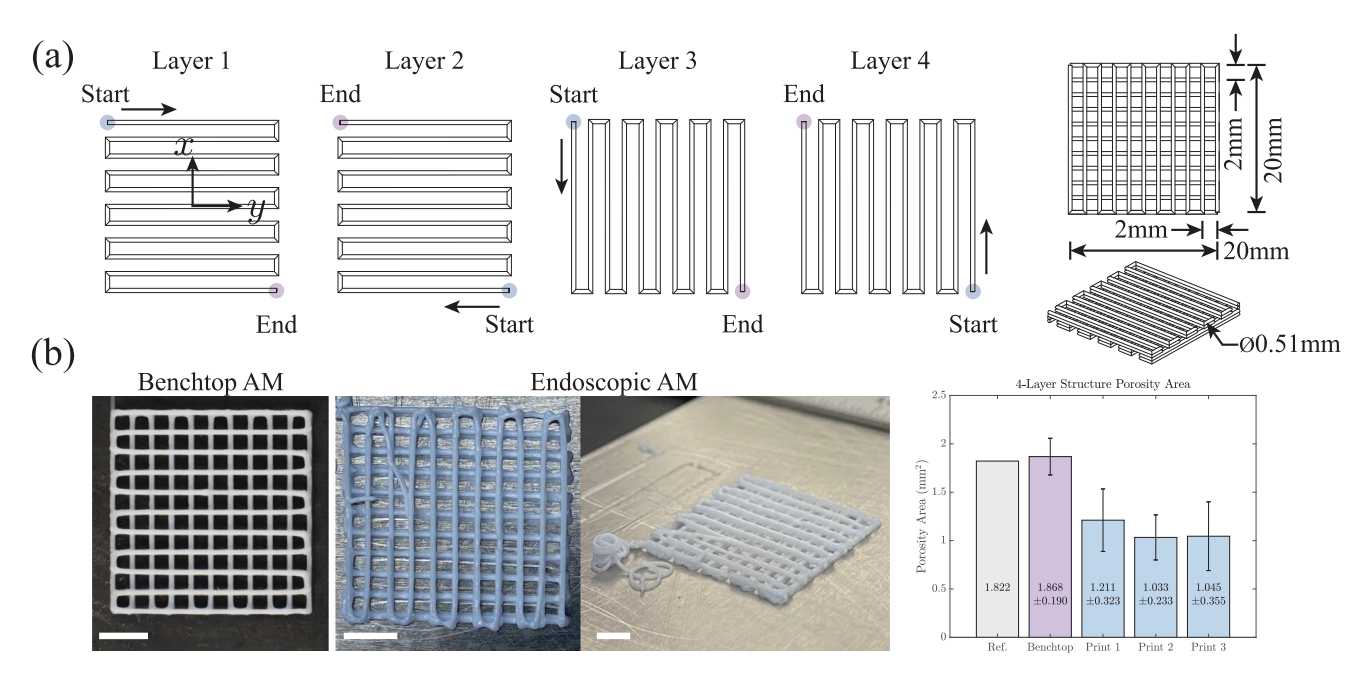


Fig. 8. Four layer lattice structures. (a) Structure design. (b) Printing results for 1 print with benchtop system and 3 prints with Endoscopic AM system. Print 1 (top-down and side view) is pictured for Endoscopic AM. Numerical results present averaged values with one standard deviation. Scale bars are 5 mm.

deviations along 1 mm vertical segments on the left and right side of the structure (Fig. 6(d)). Porosity area is measured by identifying pore boundaries in each 4-layer lattice using the Moore-Neighbor tracing algorithm [33] and calculating the area defined by identified vertices (Fig. 6(e)). Like filament width, we average positioning error and porosity area data to report scalar values per print. Statistical comparisons use the Student's t-test to test the hypothesis that there is no significant difference in the means of two different groups. If the p-value is less than 0.05 the null hypothesis is rejected and the difference between means is deemed significant.

V. RESULTS AND DISCUSSION

Intracorporeal lattice fabrication is qualitatively comparable to a benchtop system, but quantitatively 5 times less accurate. In the 1-layer lattice (Fig. 7(b)), we find in-plane errors of approximately 100 µm and 500 µm for benchtop AM and Endoscopic AM, respectively. Error differences between Endoscopic AM and benchtop AM were significant (p < 0.001), and error differences between prints of Endoscopic AM were insignificant (p > 0.05). We find Endoscopic AM produces filament widths approximately 200 µm larger than desired, indicating $\Delta z \approx 100$ µm. However, filament width differences between Endoscopic AM and benchtop AM and between prints of Endoscopic AM were insignificant (p > 0.05). In the 4-layer lattice (Fig. 8(b)), we find a 40% reduction in porosity area with Endoscopic AM due to layer misalignment and, in some instances, filament separation, which creates regions of artificially small pores. Porosity differences between Endoscopic AM and benchtop AM were significant (p < 0.001), and porosity differences between prints of Endoscopic AM were insignificant (p > 0.05). In the 1-layer lattice, we see consistent substrate adhesion with

minimal filament separation. In the 4-layer lattice, we observed larger errors in filament placement on the topmost layers due to a lack of adhesion to the previous layer. Importantly, as shown by the 4-layer structures, positioning and filament consistency errors are sufficiently small to allow for 3D structure fabrication.

Filament deposition and adhesion is an interplay of accurate positioning, flow control, and material properties in DW systems. From a process perspective, loading material in Endoscopic AM is challenging and the introduction of air bubbles into both build and hydraulic fluids is difficult to avoid. We hypothesize that process optimizations of the material loading procedure will reduce bubble entrapment and have an appreciable impact on filament fidelity. Positioning errors are a function of the accuracy of the robotic system and the calibration used to map the printing platform to $\{E\}$. The system used in this work has not undergone a kinematic parameter calibration and we expect performing such a procedure will improve both the positioning of the end effector and its positioning relative to the printing platform. Finally, we observed small vibrations when moving in the x direction of the lattices (see Supplementary Video). These motions produce bead-like structures in lattice layers and are likely due to a deviation between the physical location of the RCM and its idealized kinematic location, further supporting our assumption that kinematic calibration should be performed.

The current work is image-based and thus limits our ability to fully compare intracorporeal construct fabrication to benchtop methods for 3D structures. In future work, we plan to quantify porosity with microcomputed tomography based measurements using the methods in [29]. Flow measurements will improve filament width assessment and we plan to explore pressure based flow measurements as in [24] in subsequent works. Manufacturability in DW systems does not map directly to

TE structure acceptance by the body and cellular proliferation. Critically, the body is relatively insensitive to construct fidelity as successful cellular proliferation is possible with pore sizes 200-1600 µm [34]. Our group is currently exploring the biological needs for intracorporeal TE and planning to assess the TE capabilities of Endoscopic AM with biological studies of clinically relevant structures printed on soft tissue substrates using cell-laden biomaterials appropriate for soft tissues. Tissue-instrument interactions and motions due to body processes will be a key area of future research as deformation of soft tissue substrates poses a considerable challenge to consistent manufacturability. The present work focused on printability in a laboratory setting; considerable future work in these areas will be required to realize Endoscopic AM in the operating room.

ACKNOWLEDGMENT

The authors thank Ali Asghari Adib and Dr. Desmond D'Souza for their thoughtful discussions and insights, and help with experiments.

REFERENCES

- S. J. Hollister and W. L. Murphy, "Scaffold translation: Barriers between concept and clinic," *Tissue Eng. Part B: Rev.*, vol. 17, no. 6, pp. 459–474, 2011.
- [2] A. Atala, F. K. Kasper, and A. G. Mikos, "Engineering complex tissues," Sci. Transl. Med., vol. 4, no. 160, pp. 1–10, 2012.
- [3] I. T. Ozbolat and M. Hospodiuk, "Current advances and future perspectives in extrusion-based bioprinting," *Biomaterials*, vol. 76, pp. 321–343, 2016.
- [4] T. Billiet, M. Vandenhaute, J. Schelfhout, S. Van Vlierberghe, and P. Dubruel, "A review of trends and limitations in hydrogel-rapid prototyping for tissue engineering," *Biomaterials*, vol. 33, no. 26, pp. 6020–6041, 2012.
- [5] F. P. W. Melchels, M. A. N. Domingos, T. J. Klein, J. Malda, P. J. Bartolo, and D. W. Hutmacher, "Additive manufacturing of tissues and organs," *Prog. Polym. Sci.*, vol. 37, no. 8, pp. 1079–1104, 2012.
- [6] F. R. Arko, B. B. Hill, C. O. Iv, E. J. Harris, T. J. Fogarty, and C. K. Zarins, "Endovascular repair reduces early and late morbidity compared to open surgery for abdominal aortic aneurysm," *J. Endovascular Ther.*, vol. 9, pp. 711–718, 2002.
- [7] J. Kim, G. J. Lee, J.-H. Baek, and W.-S. Lee, "Comparison of the surgical outcomes of laparoscopic versus open surgery for colon perforation during colonoscopy," *Ann. Surg. Treat. Res.*, vol. 87, no. 3, pp. 139–143, 2014
- [8] N. C. Buchs, F. Pugin, D. E. Azagury, O. Huber, G. Chassot, and P. Morel, "Robotic revisional bariatric surgery: A comparative study with laparoscopic and open surgery," *Int. J. Med. Robot. Comput. Assist. Surg.*, vol. 10, pp. 213–217, 2014.
- [9] T. Hinoi et al., "Laparoscopic versus open surgery for colorectal cancer in elderly patients: A multicenter matched case - Control study," Ann. Surg. Oncol., vol. 22, no. 6, pp. 2040–2050, 2015.
- [10] J. Ho et al., "Laparoscopic approach for left-sided T4 colon cancer is a safe and feasible procedure, compared to open surgery," Surg. Endoscopy, vol. 33, no. 9, pp. 2843–2849, 2019.
- [11] Frost & Sullivan, "Innovations in surgical robotics (Technical Insights)," Tech. Rep. D50E-TI, Dec., 2013.
- [12] S. Pinkerton, "The pros and cons of robotic surgery," 2013. [Online]. Available: https://tinyurl.com/2p8kaazf

- [13] J. Lipskas, K. Deep, and W. Yao, "Robotic-assisted 3D bio-printing for repairing bone and cartilage defects through a minimally invasive approach," *Nature Sci. Rep.*, vol. 9, no. 1, pp. 1–9, 2019.
- [14] W. Zhao and T. Xu, "Preliminary engineering for in situ in vivo bioprinting: A novel micro bioprinting platform for in situ in vivo bioprinting at a gastric wound site," *Biofabrication*, vol. 12, no. 4, pp. 1–12, 2020.
- [15] C. Zhou et al., "Ferromagnetic soft catheter robots for minimally invasive bioprinting," *Nature Commun.*, vol. 12, no. 1, pp. 1–12, 2021.
- [16] A. Simeunović and D. J. Hoelzle, "Coupled dynamics of material delivery and robotic manipulator axes in endoscopic additive manufacturing," in *Proc. Amer. Control Conf.*, Philadelphia, PA, USA, 2019, pp. 687–692.
- [17] Y. Zhao, Y. Li, S. Mao, W. Sun, and R. Yao, "The influence of printing parameters on cell survival rate and printability in microextrusionbased 3D cell printing technology," *Biofabrication*, vol. 7, no. 4, 2015, Art. no. 045002.
- [18] R. Chang, J. Nam, and W. Sun, "Effects of dispensing pressure and nozzle diameter on cell survival from solid freeform fabrication-based direct cell writing," *Tissue Eng. Part A*, vol. 14, no. 1, pp. 41–48, 2008.
- writing," *Tissue Eng. Part A*, vol. 14, no. 1, pp. 41–48, 2008.

 [19] E. Lepowsky, M. Muradoglu, and S. Tasoglu, "Towards preserving post-printing cell viability and improving the resolution: Past, present, and future of 3D bioprinting theory," *Bioprinting*, vol. 11,pp. 1–17, 2018.
- [20] J. Shi, B. Wu, S. Li, J. Song, B. Song, and W. F. Lu, "Shear stress analysis and its effects on cell viability and cell proliferation in drop-on-demand bioprinting," *Biomed. Phys. Eng. Exp.*, vol. 4, no. 4, 2018, Art. no. 045028.
- [21] L. Ning, N. Betancourt, D. J. Schreyer, and X. Chen, "Characterization of cell damage and proliferative ability during and after bioprinting," ACS Biomaterials Sci. Eng., vol. 4, no. 11, pp. 3906–3918, 2018.
- [22] G. Guthart and J. Salisbury, "The intuitive telesurgery system: Overview and application," in *Proc. IEEE Int. Conf. Robot. Automat.*, 2000, pp. 618–621.
- [23] A. Simeunović and D. J. Hoelzle, "Nonlinear and linearized gray box models of direct-write printing dynamics," *Rapid Prototyping J.*, vol. 26, no. 10, pp. 1665–1676, 2020.
- [24] A. A. Adib and D. J. Hoelzle, "Hybrid control of flowrate in microextrusion-based direct-write additive manufacturing," *IEEE Control* Syst. Lett., vol. 6, pp. 97–102, Jan. 2022.
- [25] EtherCAT Technology Group, "EtherCAT The ethernet fieldbus," Ether-CAT Technol. Group, Nuremberg, Germany, Tech. Rep. 03/2020, 2020. [Online]. Available: https://bit.ly/3CZIgwm
- [26] Generic interface and use of profiles for power drive systems Mapping of profile type 1 to network technologies, IEC 61800-7-301:2015, International Electrotechnical Commission, Geneva, Switzerland, Nov. 20, 2015.
- [27] K. Shoemake, "Animating rotation with quaternion curves," SIGGRAPH Comput. Graph., vol. 19, no. 3, pp. 245–254, Jul. 1985.
- [28] J. M. Barnes, L. Przybyla, V. M. Weaver, and A. Ewald, "Tissue mechanics regulate brain development, homeostasis and disease," *J. Cell Sci.*, vol. 130, no. 1, pp. 71–82, 2017.
- [29] A. A. Adib et al., "Direct-write biofabrication and characterization of a GelMA-based biomaterial for intracorporeal additive manufacturing of tissue engineering scaffolds," *Biofabrication*, vol. 12, no. 4, Jul. 2020, Art. no. 045006.
- [30] J. J. Craig, Introduction to Robotics: Mechanics and Control, 4th ed. New York, NY, USA: Pearson Eduction, 2018.
- [31] R. Chhabra and J. Richardson, Non-Newtonian Flow and Applied Rheology: Engineering Applications Second Edition, 2nd ed. Oxford, U.K.: Elsevier Ltd, 2008.
- [32] L. Ouyang, C. B. Highley, C. B. Rodell, W. Sun, and J. A. Burdick, "3D printing of shear-thinning hyaluronic acid hydrogels with secondary cross-linking," ACS Biomaterials Sci. Eng., vol. 2, no. 10, pp. 1743–1751, 2016.
- [33] R. C. Gonzalez, R. E. Woods, and S. L. Eddins, *Digital Image Processing Using MATLAB*, 1st ed. Upper Saddle River, NJ, USA: Pearson/Prentice Hall, 2004.
- [34] S. J. Hollister, "Porous scaffold design for tissue engineering," *Nature Mater.*, vol. 4, pp. 518–524, 2005. [Online]. Available: http://www.ncbi.nlm.nih.gov/pubmed/16003400